PCCP

Accepted Manuscript

ROYAL SOCIETY OF CHEMISTRY

www.rsc.org/pccp

Synthesis of Palladium Nanoparticles on TiO_2(110) using a Beta-Diketonate Precursor

*Yu Lei**[†,‡], *Bin Liu*[⊥], *Junling Lu*[§], *Xiao Lin*[#], *Li Gao*[⊗], *Nathan P. Guisinger*[Ψ], *Jeffrey P. Greeley*[¶], *Jeffrey W. Elam**[†]

[†]Energy Systems Division, [Ψ]Center for Nanoscale Materials, Argonne National Laboratory, Lemont, IL 60439, USA

[‡]Department of Chemical and Materials Engineering, University of Alabama in Huntsville, Huntsville, AL 35899, USA

[⊥]Department of Chemical Engineering, Kansas State University, Manhattan, KS 66506, USA

[§]Department of Chemical Physics, Hefei National Laboratory for Physical Sciences at the Microscale, and CAS Key Laboratory of Materials for Energy Conversion, University of Science and Technology of China, Hefei 230026, China

[#]University of Chinese Academy of Sciences & Institute of Physics, Chinese Academy of Sciences, Beijing 100049, China

[⊗]Department of Physics and Astronomy, California State University Northridge, CA 91330, USA

[¶]School of Chemical Engineering, Purdue University, West Lafayette, IN 47907, USA

Abstract

The adsorption of palladium hexafluoracetylacetone ($Pd(hfac)_2$) and nucleation of Pd nanoparticles on TiO_2(110) surface were observed using scanning tunneling microscopy (STM). Surface species of Pd(hfac)* and Ti(hfac)* uniformly adsorbed on TiO_2(110) upon exposure of $Pd(hfac)_2$. No preferential nucleation was observed for the surface species. Atomic resolution STM images revealed that both Pd(hfac)* and Ti(hfac)* appeared on the metastable Ti(5c) sites. After annealing at 700 K, sub-nm Pd nanoparticles were observed across the TiO_2(110) without preferential nucleation. The adsorption preferences of Pd(hfac), hfac, and atomic Pd on TiO_2 (110) surface were studied using density functional theory (DFT), and possible decomposition pathways of $Pd(hfac)_2$ leading to the formation of Pd nucleation sites were presented.

Keywords atomic layer deposition, model catalysis, nanoparticles, organometallics, rutile TiO_2, density functional theory

Introduction

Highly dispersed supported precious metal nanoparticles in the sub-nanometer to nanometer range are of great interest in heterogeneous catalysis. Atomic layer deposition (ALD) has arisen as an alternative technique to tailor the size and composition of metal and metal oxides in this size regime, and has the advantages of growing conformal coatings of thin films and highly dispersed nanoparticles on high surface area supports, which are frequently used in catalysis.[1-6] Size- and composition-controlled heterogeneous catalysts prepared by ALD have shown their advantages in multiple catalytic applications, such as, fuel cells,[7] alkane dehydrogenation,[8] water splitting,[9] and biomass conversion.[10]

Supported palladium nanoparticles are of great interest in heterogeneous catalysis. A Pd ALD process, using palladium hexafluoroacetylacetonate ($Pd(hfac)_2$) as precursor and a reducing agent as co-reactant, e.g., formalin and hydrogen, has been developed to yield monodispersed Pd nanoparticles under mild synthesis conditions.[11-13] Nanostructured Pd catalysts prepared by this method are highly active for alkane dehydrogenation,[8, 14] lithium-O_2 battery, [15-16] methanol decomposition,[13, 17] and alcohol oxidation for fuel cells [18].

The ability to control the size and structure of Pd nanoparticles prepared by ALD relies on thorough understandings on the surface chemistry of this process. Operando characterization techniques are highlighted to probe the surface reactions under practical ALD conditions to obtain such knowledge in real time. In a combined study using *in situ* FT-IR, X-ray absorption spectroscopy (XAS), pair distribution function (PDF) and density functional theory (DFT) calculations, the adsorption and deligation of the precursor and nucleation of Pd nanoparticles on a TiO_2 surface were resolved. [19] However, the surface impurities and multiple phases of TiO_2 support may bring uncertainties to the mechanisms of the surface reactions. The understanding of

Pd ALD will be beneficent from study on a well-defined TiO_2 surface, such as TiO_2 single crystal surface.

Organometallic compounds were used as precursors to prepare well-defined model catalysts on single crystal supports. Model catalyst, typically consisting of single crystal substrate or oxide thin film and supported metal clusters, have been developed to understand the catalyst structure-reactivity relationship. [20-23] The use of surface science probes on model catalysts provides fundamental understandings of particle-support interactions, and particle size and shape effects. Pioneer work in this area was conducted in the collaboration of Goodman and Gates *et al*. [24-25] The adsorption of rhenium carbonyl species, $HRe(CO)_5$ and $Re_2(CO)_{10}$, on MgO thin films grown on Mo(110) surface were studied using combined temperature programmed desorption-reflection absorption infrared spectroscopy (TPD-RAIRS) experiments. More recently, Zaera and coworkers utilized X-ray photoelectron spectroscopy (XPS) and temperature programmed desorption (TPD) to reveal the thermal decomposition of copper(I)-*N,N'*-di-sec-butylacetamindinate on well-defined Ni(100) single crystal surface and suggested an upper temperature limit for Cu ALD process.[26] A thorough XPS study on thermal decomposition of $Pd(hfac)_2$ on rutile $TiO_2(110)$ surface were reported by Zemlyanov and coworkers.[27] The oxidation state of Pd gradually decreasing from Pd^{2+} to Pd^0 was observed upon thermal decomposition. However, an important question that arose from the above works is the structural relationship between the adsorbed precursor and the support.

The development of scanning tunneling microscopy (STM) enables direct observation of the adsorption of organometallic compounds and nucleation of metal and metal oxides. The adsorption behavior of $Ru_3(CO)_9(Sn(C_6H_5)_2)_3$ was studied on $SiO_2/Mo(112)$[28] and $Al_2O_3/Ni_3Al(111)$[29], respectively. A two dimensional triangle Ru_3Sn_3 cluster was formed on SiO_2

surface simultaneously after ligands removal. The adsorption of Rh beta-diketonate precursors and nucleation of Rh clusters on $Al_2O_3/Ni_3Al(111)$[30-31], $Al_2O_3/NiAl(110)$[32] and $TiO_2(110)$[33] were also studied, respectively. The adsorption behavior of Rh precursors and the nucleation of nanoparticles highly depend on the choices of support materials and organometallic precursors.

A unique technique likely to consummate effective and viable understandings of organometallic adsorbates and support interaction, STM were brought into the investigation of the early ALD steps under UHV conditions. Kummel and coworkers studied the reactions of trimethyl aluminum (TMA) over GaAs(001) and InGaAs(001) surfaces, and found uniform adsorption of intermediate species dimethyl alumina (DMA). [34] More recently, an *in situ* STM study performed by Prinz and coworkers on ZnS ALD on Au(111) surface revealed that the nucleation of ZnS and the surface morphology change with increasing number of ALD cycles. [35]

In this work, we employed STM and DFT calculations to investigate the adsorption of $Pd(hfac)_2$ and nucleation of Pd nanoparticles on a rutile $TiO_2(110)$ surface. The precursor initial adsorption and resultant nanoparticles are atomically visualized under the UHV conditions.

Results and Discussion

Figure 1 shows a clean rutile $TiO_2(110)$ surface with surface hydroxyl groups OH and oxygen vacancies (O_v). In Figure 1a, different layers of the surface show an average step height of ~3.3 Å, consistent with the step height of $TiO_2(110)$.[36] Well oriented row structure of rutile $TiO_2(110)$ surface and surface features can be clearly seen in Figure 1b. The sample was positively biased at 1.0-2.0 V relative to the STM tips, allowing electron tunneling into unoccupied states of the sample. Under these conditions, the bright rows are assigned to five-fold coordinated titanium Ti(5c) atoms alternating with dark rows corresponding to 2-fold coordinated bridging oxygen O(2c) atoms protruding on the surface. As shown in Figure 1b and

1c, the distance between the dark rows is 6.5 Å, consistent with a (1×1) surface unit cell. The bright spot on O(2c) row is surface OH, while the O_v appears as a dim spot on O(2c) row. The surface OH and O_v have apparent heights of ~1.5 Å and ~1.0 Å, respectively. Similar to the observation by Wendt *et al.* [37] and Park *et al.* [38], the apparent height of the surface OH is higher than the height of O_v. The density of surface O_v for the fresh sample is counted as 3.2×10^{12} cm^{-2}.

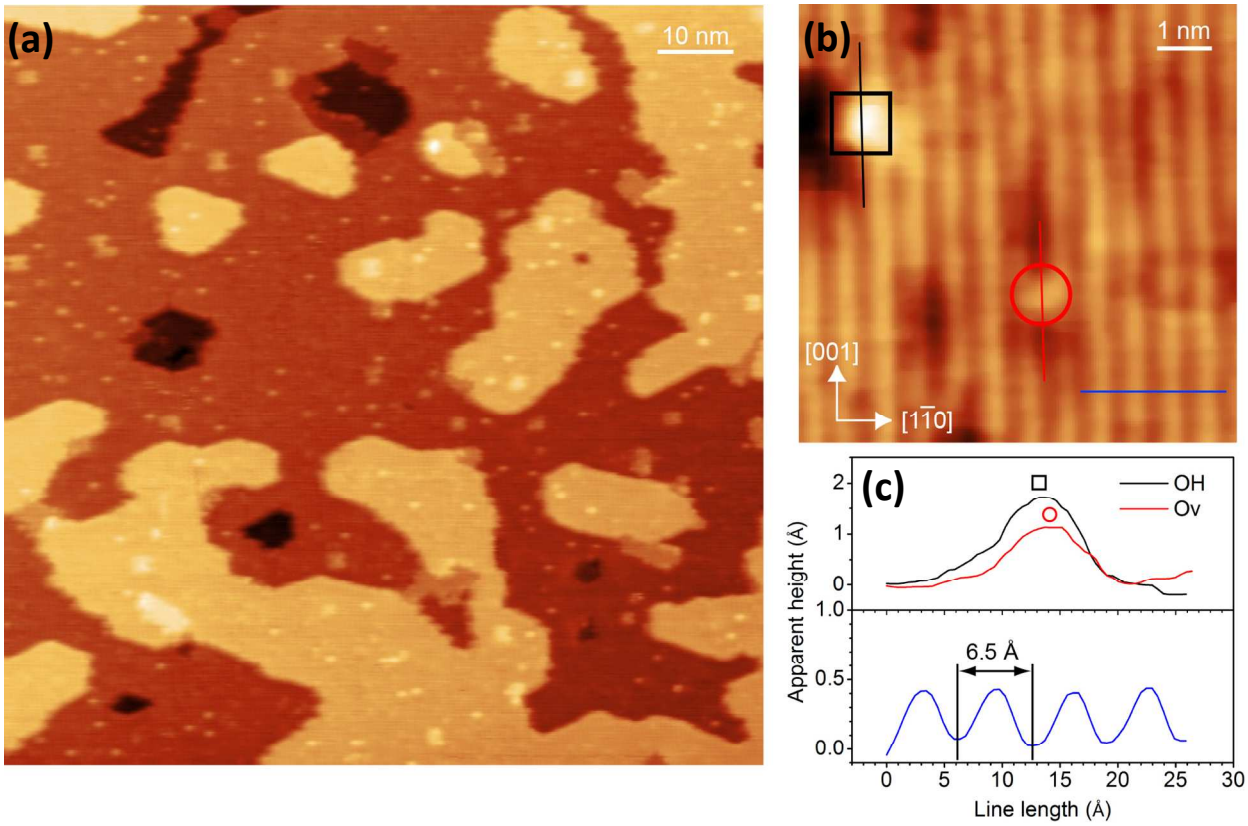

Figure 1. STM images of (a) clean rutile TiO_2(110) surface, 100 nm × 100 nm. (b) surface O_v sites and OH groups, 8.0 nm × 8.0 nm. (c) Apparent height of surface features. Bias voltage: 1.0 V. Tunneling current 0.15 nA. *Black square*, OH group. *Red circle*, O_v site. Blue line, line profile of TiO_2 surface.

$Pd(hfac)_2$ precursors were exposed to the clean TiO_2(110) surface in a separated preparation chamber. Though *in situ* STM study could closely follow the change of surface

morphology during ZnS ALD in the study by Mack *et al*.,[35] exposure precursors in the STM chamber could simultaneously grow ALD thin films on the STM tips, giving rise to different STM tip conditions and leading to questionable, sometimes even reversed results. In addition, unexpected changes of tip conditions could happen on TiO_2(110) surface as the STM tip easily picks up an oxygen atom from the TiO_2, making O(2c) sites appearing as bright row or leading to "super resolution" due to double-tip effect.[36] Care is taken in this study where only images obtained under normal tip conditions are used. All the images shown in this work have a (1x1) surface unit cell and surface OH and O_v lay on the O(2c) sites (dark row).

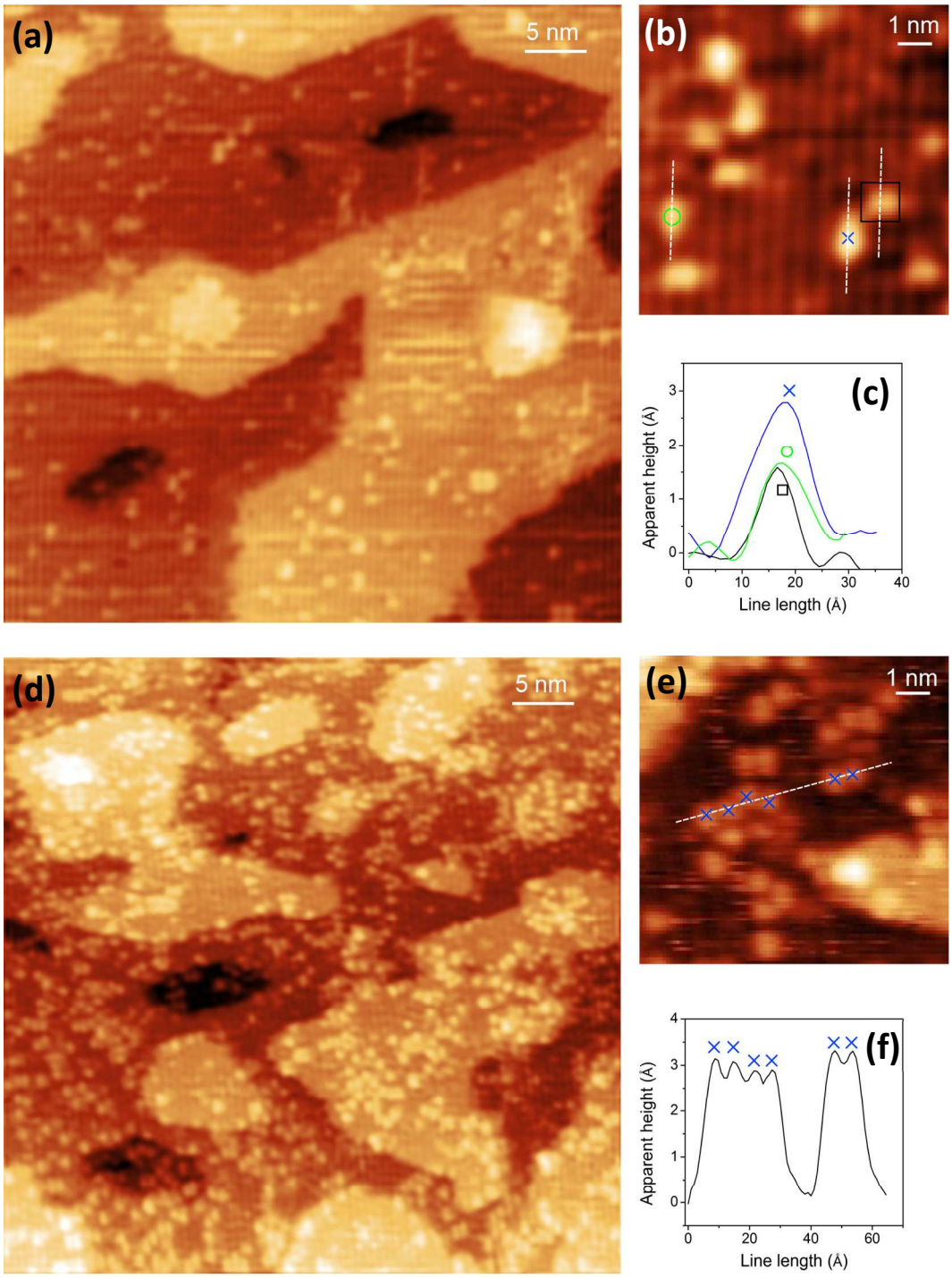

Figure 2. STM image of (a) and (b) Pd(hfac)* coverage of 3.8×10^{12} cm^{-2}, (d) and(e) Pd(hfac)* coverage of 2.2×10^{13} cm^{-2}. (c) line profile of the surface species shown in (b). (f) line profile of the surface species shown in (e). (a) and (d), 50 nm × 50 nm. (b) and (e), 9 nm × 9 nm. Bias voltage: 2V. Tunneling current 0.2 nA. *Black square*, OH groups. *Blue cross*, Pd(hfac)*. *Green circle*, Ti(hfac)*.

In the Pd ALD process using $Pd(hfac)_2$ as precursor, substrate was typically heated to between 373 K to 473 K to ensure monolayer chemisorption and self-limiting reaction.[11, 19] Analogy to the practical condition, the exposure of $Pd(hfac)_2$ to $TiO_2(110)$ surface was performed when $TiO_2(110)$ was kept at 373 K. Figure 2 shows the $TiO_2(110)$ surface after $Pd(hfac)_2$ exposure resulting in different surface coverage. There is no preferential nucleation at the step edges. Similarly, no preferential nucleation was observed when Sterrer and coworkers used $PdCl_2$ as precursor to prepare Pd nanoparticles on thin $Fe_3O_4(111)$ films in a solution approach. [39] On the other hand, precious metal single atoms and nanoparticles such as Pd, Pt, and Au generated by physical vapor deposition (PVD) were found preferentially nucleate on the step edge of $TiO_2(110)$. [38, 40] This difference between metal deposition using a chemical precursor versus by PVD can be ascribed to the homogeneous dispersion of the adsorbed precursors.

Figure 2b exhibits a higher resolution STM image showing the morphology of $TiO_2(110)$ surface at low coverage. Compared to clean $TiO_2(110)$ surface, besides OH showing as bright spots on O(2c) rows with an apparent height of 1.5 Å, there are two new types of bright spots adsorbed on the Ti(5c) sites (bright row). Line profiles across these two species in Figure 2c show that the two new surface species have apparent heights of ~1.5 Å and ~3 Å, which are assigned to Ti(hfac)* and Pd(hfac)*, respectively. The formation of surface Ti(hfac)* and Pd(hfac)* after $Pd(hfac)_2$ exposure have been identified as the only two new surface species using *in-situ* FT-IR performed under practical Pd ALD conditions. [19] These surface species are thermally stable at 200 °C, consistent with the self-limiting nature of ALD. The bright dot with ~1.5 Å apparent height is likely to be the hfac ligands deligated from $Pd(hfac)_2$ precursor and spilled-over on Ti(5c) sites (bright row). Though surface OH (black square) also had an apparent

height of ~1.5 Å on the clean TiO_2(110) surface, it can be clearly distinguished from Ti(hfac)* (green circle) in Figure 2b as surface OH appeared only on the O(2c) sites (dark row).

Pacchioni and coworkers, stating that Pd monomers would preferentially adsorb on protruding O(2c) sites. [41] Similarly, the Pd(hfac)* (blue cross) species are expected to adsorb on TiO_2 through Ti-O-Pd bonds and observed on O(2c) sites. However, the Pd(hfac)* with apparent height of ~3 Å seemed to center on the Ti(5c) sites, which was contradictive to what we predicted from DFT calculations discussed below where Pd(hfac)* was also found to adsorb on O(2c) sites. One possible reason is that Pd(hfac)/Ti(5c) might be a metastable state. At the deposition temperature 373 K, it was kinetically easier for the Pd(hfac) to reach this metastable state (on Ti(5c)) than the stable state (on O(2c)). At the same time, the energy of the Pd(hfac)* is not large enough to overcome the barrier between the metastable state and the thermodynamically favorable state, which makes the Pd(hfac)* appear at the metastable state in STM images measured at room temperature. By counting only the species with apparent height of ~3 Å, the surface coverage of Pd(hfac)* can be determined as 3.8×10^{12} cm^{-2}. A surface with higher coverage of 3.5×10^{13} cm^{-2} Pd(hfac)* is shown in Figure 2d and 2e where the population of Pd(hfac)* with apparent height ~3 Å significantly increased.

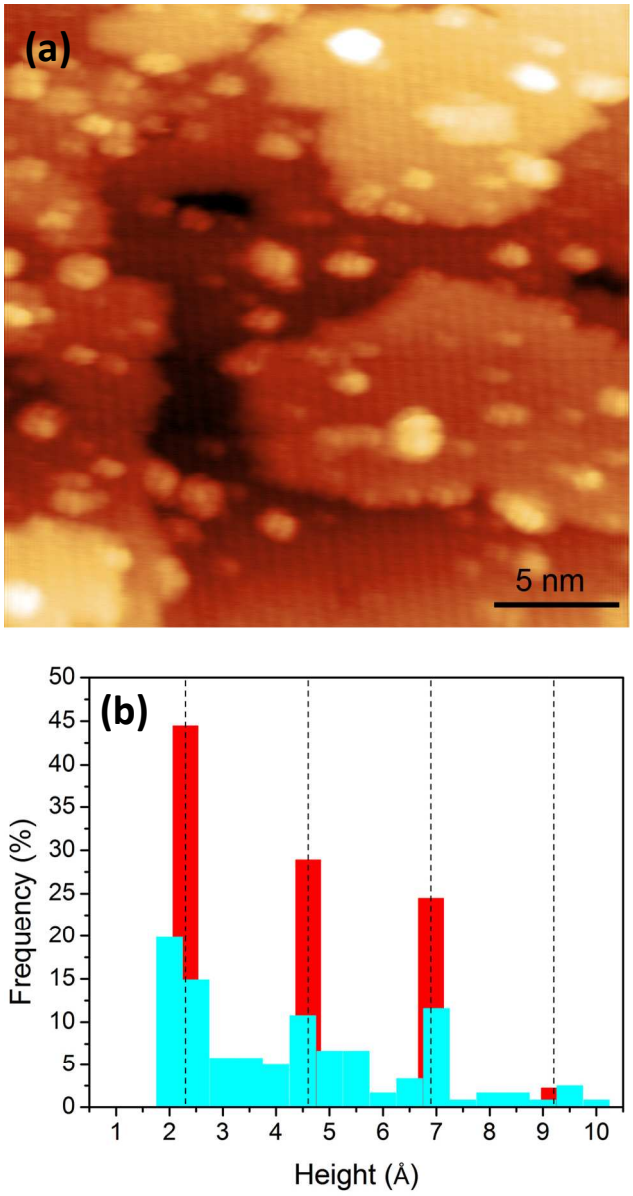

Figure 3. (a) STM image of Pd nanoparticles on rutile TiO_2(110) surface after annealing at 700 K in UHV. 25 nm × 25 nm. Bias voltage: 1.3 V. Tunneling current 0.3 nA. (b) Surface particles height distribution. Vertical dash lines represent the Pd-Pd step height. *Cyan*, surface particles size distribution. *Red*, Pd nanoparticles size distribution.

The Pd(hfac)*/TiO_2(110) sample was annealed in UHV at 700 K for 10 minutes to allow the surface species to fully decompose. *In situ* XPS study showed that Pd(hfac)* thermally

decomposed between 575 and 775 K with the Pd $3d_{5/2}$ peak shifted from 336.2 eV to 335.8 eV. [27] In addition, the surface is most likely to be stoichiometric TiO_2 which accounts for more than 93% of the surface during the whole annealing process. With the thermal decomposition of Pd(hfac)*, Pd nanoparticles were observed on TiO_2(110) surface shown in Figure 3a. The particles spread out uniformly across the surface on both terrace and the step edge. By including only those particles larger than 0.5 nm in diameter and higher than 0.2 nm in height, surface particle density decreased to 1.7×10^{13} cm^{-2} after 700 K annealing. The cyan bar in Figure 3b shows an apparent height distribution of the surface particles. Pd atomic balance before and after annealing can be used to determine whether the particles shown in Figure 3a are all Pd nanoparticles. By simply assuming all the particles are in hemispherical shape, the Pd atom density would have been ~1.9×10^{14} cm^{-2} should all the particles shown in Figure 3a be Pd. Since the initial Pd(hfac)* surface coverage was only ~3.5×10^{13} cm^{-2}, it is obvious that not all the particles shown in Figure 3a are Pd nanoparticles. Pd(111) surface has a step height of 2.3 Å and it is compared with the particles height in Figure 3b. If only considering particles with an apparent height near 2.3 Å, 4.6 Å, 6.9 Å and 9.2 Å (± 0.3 Å) as Pd nanoparticles, the Pd atom density can be calculated as ~3.5×10^{13} cm^{-2}, similar to the Pd atom density obtained from the Pd(hfac)*/TiO_2(110) surface. The red bars in Figure 3b shows the size distribution of Pd nanoparticles with mean height of ~4.2 Å. The rest of the particles could be surface carbon species formed from thermal decomposition of hfac ligands, which were reported as surface residuals from previous studies using FT-IR [42] and XPS [11, 27].

The decomposition of $Pd(hfac)_2$ can be written as Rxn (1) and (2). The asterisk symbol represent open surface, as defined below for E_{surf}.

$$Pd(hfac)_2(g) + 2* \rightarrow Pd(hfac)* + hfac* \qquad \text{Rxn (1)}$$

$$Pd(hfac)* + * \rightarrow Pd* + hfac* \qquad \text{Rxn (2)}$$

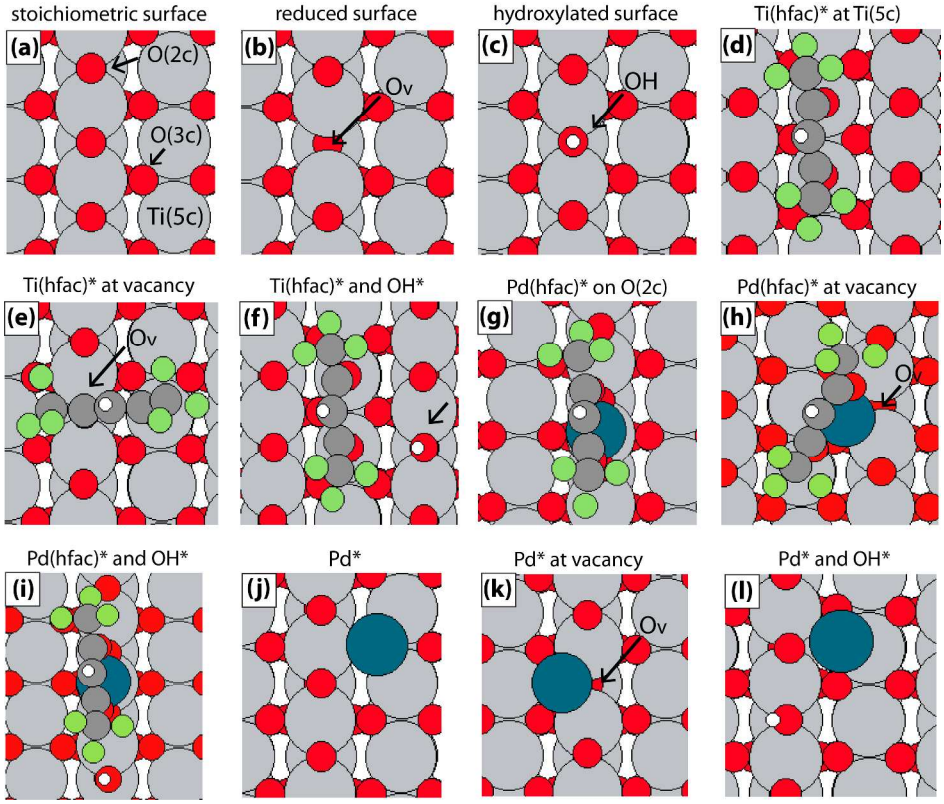

Figure 4. Adsorption configurations of TiO_2 surface and $Pd(hfac)_2$ decomposition intermediates. (a) stoichiometric TiO_2(110), (b) reduced surface with O_v sites (indicated by the arrow), (c) hydroxylated surface (indicated by the arrow), (d) Ti(hfac)*, (e) Ti(hfac)* at O_v, (f) Ti(hfac)* and OH*, (G) Pd(hfac)*, (h) Pd(hfac)* at O_v, (i) Pd(hfac)* and OH*, (j) Pd atom, (k) Pd atom at O_v, and (l) Pd atom near the OH group. Black arrows indicate O_v. Large grey spheres represent Ti, red spheres represent O, white spheres represent H, small dark grey spheres represent C, green spheres represent Cl, and blue spheres represent Pd. The O(2c), O(3c), and Ti(5c) sites are labeled in A.

Figure 4a-c illustrates the respective model TiO_2 surfaces, i.e., stoichiometric, reduced (with one O_v vacancy site), and dydroxylated (O_v occupied by a hydroxyl group) model surfaces

for DFT calculations. While the reduced and hydroxylated TiO_2 surfaces are common under experimental conditions, the stoichiometric surface model was used as a reference surface for the purpose of comparison in this study. The O(2c), which indicates the bridging O atom, and the 5-coordinated surface Ti atom, the Ti(5c) site, are labeled in Figure 4a.

The first step of decomposition produces Pd(hfac)* and the hfac* ligand. Using the gas phase $Pd(hfac)_2$ and clean surface as the reference, the generic form of the reaction energy for Rxn (1) is written as: $\Delta E_{Rxn(1)} = E_{Pd(hfac)*} + E_{hfac*} - 2E_{surf} - E_{Pd(hfac)2(g)}$, where 'surf' is used to generally represent all three surface conditions of TiO_2(110), i.e., the stoichiometric, reduced surface, and hydroxylated state. In order to elucidate the decomposition at different surface conditions, we assume that the surface is either stoichiometric, or reduced/hydroxylated (but not both). Although it is possible that the surface may possess both O_v site and hydroxyl group, we will not report those results in this work. The lowest reaction energies for each type of surfaces for Rxn (1) are: 1.19 eV (stoichiometric), -1.99 eV (reduced), and -0.91 eV (hydroxylated) as summarized in Table 1.

Table 1. Reaction energies for Rxn (1) and Rxn (2) from DFT calculations with U = 0 eV and U = 4.2 eV.

	Stoichiometric		**Reduced**		**Hydroxylated**	
	U = 0 eV	U = 4.2 eV	U = 0 eV	U = 4.2 eV	U = 0 eV	U = 4.2 eV
Rxn (1)	1.38	1.19	-0.80	-1.99	-0.44	-0.91
Rxn (2)	2.09	1.50	-0.38	-1.68	0.11	-0.81

DFT calculations also help reveal the adsorption states of the reaction species. On the stoichiometric surface, the dissociated hfac* ligand adsorbs via its carboxyl groups on two neighboring Ti(5c) sites as illustrated in Figure 4d. A similar adsorption configuration has been noted for the adsorption of formic acid, which also has the -C=O functional group in the

carboxyl group, as reported by Ahdjoudj. [43] On the stoichiometric surface, Pd(hfac)* prefers the bridge site between two O(2c) atoms so that the Pd can bond with two neighboring O atoms in the O(2c) sites as shown in Figure 4g. The coordination configuration in Pd(hfac)* is preserved with a coordination number of 4 on the central Pd atom in a planar geometry, similar to the gas phase $Pd(hfac)_2$ precursor. [19] The perpendicular height of Pd(hfac)* measured from the highest point to the O(2c) is approximately 6 Å. The discrepancy from STM measurements is, again, an indication that Pd(hfac)* is more likely adsorbing on surface defect sites resulting in lower heights. Rxn (1) on the stoichiometric surface is highly endothermic, which is 1.38 eV, indicating that the first step decomposition of $Pd(hfac)_2$ on the stoichiometric TiO_2 surface (without defects) can be very thermodynamically unfavorable.

On the reduced TiO_2 surface, one of the carboxyl groups in hfac* occupies the O_v site, with the other O in the carboxyl group staying on the Ti(5c) site as shown in Figure 4e. With the presence of O vacancy site, Pd(hfac)* also prefers to adsorb near the O_v site as shown in Figure 4h, where the Pd site adsorb off the O(2c) row in the tilted position that can lowers the molecular height observed in the STM measurements. The reaction energy for Rxn(1) becomes -1.99 eV, much more exothermic compared the stoichiometric surface (1.19 eV), and making the decomposition at O_v sites much more favorable.

On hydroxylated surfaces, where the O_v site is occupied by the hydroxyl group, hfac* again can only adsorb on two adjacent Ti top sites (Figure 4f). However, the energetics based on DFT calculations shows that hfac* becomes more stable in the presence of such OH* groups. Experimentally, the surface hfac* group has been identified on the Ti(5c) sites. This indicates that the OH* on the hydroxylated surface plays an important role in stabilizing the hfac* groups. The presence of OH* group, as shown in Figure 4i, does not play as a significant role on the

Pd(hfac)* group, as DFT calculations show that Pd(hfac)* prefers to stay away from the OH* species. The lowest reaction energy for Rxn (1) on hydroxylated surface is exothermic by -0.91 eV. Thermodynamically, this pathway is also possible.

The second decomposition step produces atomic Pd and a second hfac* ligand. The reaction energies for the second decomposition step can be written as: $\Delta E_{Rxn(2)} = E_{Pd^*} + E_{hfac^*} - E_{surf} - E_{Pd(hfac)^*}$. On the stoichiometric surface, Pd* only slightly favors the O(3c) site as illustrated in Figure 4j and will be used for our analysis in this work. Adsorption of Pd between two O(3c) sites was also studied, and the energy difference between these two configurations is negligible. This trend is reasonably consistent with Sanz and Marquez's calculations. [44] On stoichiometric surface, the reaction energy for Rxn (2) is 1.50 eV, which is also endothermic as Rxn (1) on the same surface. Figure 4k and 4l show the Pd* adsorptions on reduced and hydroxylated surfaces, respectively. On the reduced surface, Pd adsorbs off the O(2c) row between the two O(3c) sites and next to the O_v. On the hydroxylated surface, Pd also adsorbs between the O(3c) sites. The reaction energies for Rxn (2) on reduced and hydroxylated surfaces are -1.68 eV and -0.81 eV, respectively.

$Pd(hfac)_2$ decompositions on different $TiO_2(110)$ surfaces are summarized in Figure 5. It can be clearly seen that both O_v and OH* species play a significant role in assisting the deligation significantly. On the terrace sites, Rxn (1) should take place either at the O_v sites or near OH* groups so that the dissociated hfac* ligand can be stabilized. Similarly, surface defect sites or OH* species are also necessary to facilitate Rxn (2), which also generates one hfac* ligand and atomic Pd, which are stabilized by O_v and OH* and will serve as nucleation sites for Pd cluster growth.

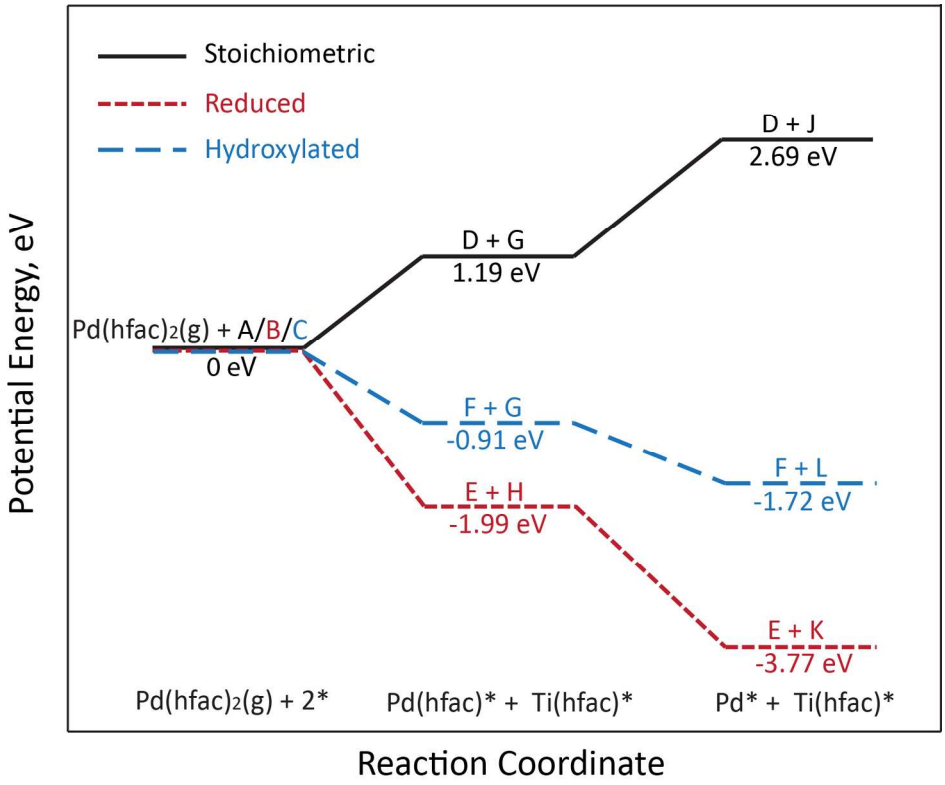

Figure 5. Potential energy surfaces the lowest energy pathways on stoichiometric (black solid line), reduced (red, short-dashed line), and hydroxylated (blue, long-dashed line) surfaces. Asterisks represent surface species. The alphabet labels at each reaction step correspond to Figure 4.

In the practical ALD operation, the Pd ALD is oftentimes performed on hydroxylated TiO_2 surface unless special pretreatment is preformed prior to Pd ALD, e.g., high temperature calcination in vacuum, which will generate slightly reduced TiO_2 surface. Though it was initially believed that surface hydroxyl groups on Al_2O_3 directly involved in the surface reaction of Pd ALD,[11] later *in situ* FT-IR studies suggested otherwise.[45] In a separated study, Feng *et al.* annealed Al_2O_3 surface to 873 K prior to Pd ALD in the hope to decrease the loading of Pd.[17] However, with a decrease of ~80% surface OH* groups, the loading of Pd only declined ~24%.

One possible reason is that OH* groups are not the attachment points of $Pd(hfac)_2$ in the surface reaction, as indicated by our DFT calculations on rutile $TiO_2(110)$ surface, but only assisted the decomposition of $Pd(hfac)_2$. On the other hand, surface OH* groups are important for practical Pd ALD as they stabilize the adsorbed Pd(hfac)* surface species. Although our results were obtained for $TiO_2(110)$ surface, the effects of surface OH* and O_v are probably universal for Pd ALD on most the oxide surfaces using $Pd(hfac)_2$ as the precursor.

Conclusion

In conclusion, when $Pd(hfac)_2$ was exposed to $TiO_2(110)$ surface at 373 K, $Pd(hfac)_2$ readily decomposed and forming two surface species: Pd(hfac)* and hfac*, both of which preferentially adsorbed on the Ti(5c) sites captured by STM at room temperature. No preferential nucleation of Pd(hfac)* was observed on $TiO_2(110)$. High temperature annealing leaded to decomposition of the surface species and formation of Pd nanoparticles, as well as surface residuals. DFT calculations were performed to provide additional insights to elucidate the $Pd(hfac)_2$ precursos decompositions and Pd nucleation site formations. The results not only reveal the most stable configurations of the key intermediate species, but also confirm the significant role of O_v and OH* species in stabilizing the dissociated ligands and Pd nucleation sites.

Experimental Methods and Theoretical Calculations

STM studies were performed in an ultrahigh vacuum variable temperature scanning tunneling microscope (VT-SPM, Omicron) and a separate preparation chamber equipped with a low-energy electron diffraction (LEED) system. A typical base pressure for the system is $\leq 1 \times 10^{-10}$ mbar. A single side polished rutile $TiO_2(110)$ single crystal ($10\times10\times1$ mm^3, Crystal GmbH) was mounted on a standard tantalum sample plate from Omicron with a 8 mm diameter hole cut in the back to facilitate heating. The temperature was previously calibrated with a type K thermocouple welded to the edge of tantalum sample plate. The clean $TiO_2(110)$ surface was prepared by repeated cycles of Ar^+ ion sputtering (1.0 keV, 4 μA) at room temperature for 20 min, with subsequent annealing at 900 K for 30 min. Surface crystallinity was confirmed with LEED and STM.

The rutile $TiO_2(110)$ surface was exposed to $Pd(hfac)_2$ (99%, Alrich) in the preparation chamber using a similar system described elsewhere.[30] The vapor of $Pd(hfac)_2$ was delivered to the $TiO_2(110)$ surface at room temperature in the preparation chamber via a leak valve and a stainless steel tube with a 1 cm inner diameter. The vapor pressure of $Pd(hfac)_2$ is 13.7 mbar at 298 K. To ensure surface self-limiting reaction and avoid precursor physisorption, the depositions were performed with the $TiO_2(110)$ crystal heated at 373 K.

STM images were collected with homemade W tips with a sample bias voltage of 1.0-2.0 V and a tunneling current of 0.1-0.3 nA. All images were generated at room temperature. Multiple images were taken and measured to obtain reasonable statistics. Care was taken to count and measure particles larger than 0.5 nm in diameter and higher than 0.1 nm in height to obtain size distribution.

Density functional theory (DFT) calculations on periodic, rutile TiO_2(110) surface were performed using the Vienne Ab Initio Simulation Package (VASP).[46-47] The projector-augmented wave (PAW) pseudopotential method was used to treat core electrons.[48-49] The energy cutoff up to 400 eV was used for the plane-wave basis set. The GGA Perdew-Burke-Ernzerhof (PBE) functional was used for the electronic exchange correlation interactions.[50] The Methfessel-Paxton smearing scheme was used, with a smearing parameter of 0.2.[51] A Monkhorst-Pack scheme with a *k*-point mesh of 2 × 2 × 1was used for the Brillouin zone sampling.[52]

The same 4-layer TiO_2(110) slab, which has a dimension of 11.76 Å in the [001] direction, and 13.06 Å in the [1$\bar{1}$0] direction as reported in our previous study,[19] was used to model the TiO_2 support. Two successive slabs are separated along the [110] direction by a vacuum of 30 Å. The top two layers were allowed to relax during the optimization of surface adsorbates, and the optimizations were considered converged when the force on each atom was less than 0.03 eV/ Å. DFT+U calculations were performed on the reduced TiO_2(110) surface (containing O vacancy), where the U parameter is set empirically to be 4.2 eV. [53] The effects of U parameter on reaction energies are shown in Table 1. Without U parameters the overall reaction energies are less exothermic, however, the final conclusions are not affected. The gas phase species, such as $Pd(hfac)_2$, and the hfac ligand, were treated in a large box with dimensions of 25.0 Å × 25.0 Å × 24.0 Å during structural optimizations. For gas phase calculations, gamma k-point sampling was used with and other DFT parameters remaining the same.

Corresponding Author

* Email: jelam@anl.gov (J.W.E.); yu.lei@uah.edu (Y.L.)

Phone: 1-630-252-3520 (J.W.E.); 1-256-824-6527 (Y.L.)

ACKNOWLEDGEMENTS

This material is based upon work supported as part of the Institute for Atom-efficient Chemical Transformations (IACT), an Energy Frontier Research Center funded by the U.S. Department of Energy, Office of Science, Office of Basic Energy Sciences. Use of the Center for Nanoscale Materials was supported by the U. S. Department of Energy, Office of Science, Office of Basic Energy Sciences, under Contract No. DE-AC02-06CH11357 and user proposal CNM 24735. The authors acknowledge grants of computer time from EMSL, a national scientific user facility located at Pacific Northwest National Laboratory, NERSC, the user facility located at Lawrence Berkeley National Laboratory and the Argonne Laboratory Computing Resource Center (LCRC). We thank Zhu Liang at University of Illinois at Chicago and Bing Yang at Argonne National Laboratory for the discussions.

REFERENCES

(1) Puurunen, R. L., *J. Appl. Phys.* **2005,** *97* (12), 121301-121352.

(2) Leskela, M.; Ritala, M., *Angew. Chem., Int. Ed.* **2003,** *42* (45), 5548-5554.

(3) Marichy, C.; Bechelany, M.; Pinna, N., *Adv. Mater.* **2012,** *24* (8), 1017-1032.

(4) Elam, J. W.; Dasgupta, N. P.; Prinz, F. B., *MRS Bull.* **2011,** *36* (11), 899-906.

(5) Parsons, G. N.; George, S. M.; Knez, M., *MRS Bull.* **2011,** *36* (11), 865-871.

(6) Zaera, F., *J. Phys. Chem. Lett.* **2012,** *3* (10), 1301-1309.

(7) King, J. S.; Wittstock, A.; Biener, J.; Kucheyev, S. O.; Wang, Y. M.; Baumann, T. F.; Giri, S. K.; Hamza, A. V.; Baeumer, M.; Bent, S. F., *Nano Lett.* **2008,** *8* (8), 2405-2409.

(8) Lu, J. L.; Fu, B. S.; Kung, M. C.; Xiao, G. M.; Elam, J. W.; Kung, H. H.; Stair, P. C., *Science* **2012,** *335* (6073), 1205-1208.

(9) Lin, Y. J.; Xu, Y.; Mayer, M. T.; Simpson, Z. I.; McMahon, G.; Zhou, S.; Wang, D. W., *J. Am. Chem. Soc.* **2012,** *134* (12), 5508-5511.

(10) Pagan-Torres, Y. J.; Gallo, J. M. R.; Wang, D.; Pham, H. N.; Libera, J. A.; Marshall, C. L.; Elam, J. W.; Datye, A. K.; Dumesic, J. A., *ACS Catal.* **2011,** *1* (10), 1234-1245.

(11) Elam, J. W.; Zinovev, A.; Han, C. Y.; Wang, H. H.; Welp, U.; Hryn, J. N.; Pellin, M. J., *Thin Solid Films* **2006,** *515* (4), 1664-1673.

(12) Lu, J. L.; Stair, P. C., *Langmuir* **2010,** *26* (21), 16486-16495.

(13) Feng, H.; Elam, J. W.; Libera, J. A.; Setthapun, W.; Stair, P. C., *Chem. Mater.* **2010,** *22* (10), 3133-3142.

(14) Lei, Y.; Liu, B.; Lu, J. L.; Lobo-Lapidus, R. J.; Wu, T. P.; Feng, H.; Xia, X. X.; Mane, A. U.; Libera, J. A.; Greeley, J. P.; Miller, J. T.; Elam, J. W., *Chem. Mater.* **2012,** *24* (18), 3525-3533.

(15) Lei, Y.; Lu, J.; Luo, X.; Wu, T. P.; Du, P.; Zhang, X. Y.; Ren, Y.; Wen, J.; Miller, D. J.; Miller, J. T.; Sun, Y. K.; Elam, J. W.; Amine, K., *Nano Lett.* **2013,** *13* (9), 4182-4189.

(16) Lu, J.; Lei, Y.; Lau, K. C.; Luo, X.; Du, P.; Wen, J.; Assary, R. S.; Das, U.; Miller, D. J.; Elam, J. W.; Albishri, H. M.; El-Hady, D. A.; Sun, Y. K.; Curtiss, L. A.; Amine, K., *Nat. Comm.* **2013,** *4*, 2383.

(17) Feng, H.; Libera, J. A.; Stair, P. C.; Miller, J. T.; Elam, J. W., *ACS Catal.* **2011,** *1* (6), 665-673.

(18) Rikkinen, E.; Santasalo-Aarnio, A.; Airaksinen, S.; Borghei, M.; Viitanen, V.; Sainio, J.; Kauppinen, E. I.; Kallio, T.; Krause, A. O. I., *J. Phys. Chem. C* **2011,** *115* (46), 23067-23073.

(19) Lei, Y.; Lu, J. L.; Zhao, H. Y.; Liu, B.; Low, K. B.; Wu, T. P.; Libera, J. A.; Greeley, J. P.; Chupas, P. J.; Miller, J. T.; Elam, J. W., *J. Phys. Chem. C* **2013,** *117* (21), 11141-11148.

(20) Baumer, M.; Freund, H. J., *Prog. Surf. Sci.* **1999,** *61* (7-8), 127-198.

(21) Goodman, D. W., *Chem. Rev.* **1995,** *95* (3), 523-536.

(22) Campbell, C. T., *Surf. Sci. Rep.* **1997,** *27* (1-3), 1-111.

(23) Henry, C. R., *Surf. Sci. Rep.* **1998,** *31* (7-8), 235-325.

(24) Purnell, S. K.; Xu, X.; Goodman, D. W.; Gates, B. C., *Langmuir* **1994,** *10* (9), 3057-3062.

(25) Purnell, S. K.; Xu, X.; Goodman, D. W.; Gates, B. C., *J. Phys. Chem.* **1994,** *98* (15), 4076-4082.

(26) Ma, Q.; Guo, H. S.; Gordon, R. G.; Zaera, F., *Chem. Mater.* **2011,** *23* (14), 3325-3334.

(27) Gharachorlou, A.; Detwiler, M. D.; Nartova, A. V.; Lei, Y.; Lu, J. L.; Elam, J. W.; Delgass, W. N.; Ribeiro, F. H.; Zemlyanov, D. Y., *ACS Appl. Mater. Interfaces* **2014,** *6*, 14702-14711.

(28) Yang, F.; Trufan, E.; Adams, R. D.; Goodman, D. W., *J. Phys. Chem. C* **2008,** *112* (37), 14233-14235.

(29) Uhl, A.; Lei, Y.; Khosravian, H.; Becker, C.; Wandell, K.; Adams, R. D.; Trenary, M.; Meyer, R. J., *J. Phys. Chem. C* **2010,** *114* (40), 17062-17068.

(30) Lei, Y.; Uhl, A.; Becker, C.; Wandelt, K.; Gates, B. C.; Meyer, R.; Trenary, M., *Phys. Chem. Chem. Phys.* **2010,** *12* (6), 1264-1270.

(31) Khosravian, H.; Lei, Y.; Uhl, A.; Trenary, M.; Meyer, R. J., *Chem. Phys. Lett.* **2013,** *555*, 7-11.

(32) Chen, Z. W.; Fujita, S.; Fukui, K., *J. Phys. Chem. C* **2011,** *115* (29), 14270-14277.

(33) Khosravian, H.; Liang, Z.; Uhl, A.; Trenary, M.; Meyer, R., *J. Phys. Chem. C* **2012,** *116* (22), 11987-11993.

(34) Clemens, J. B.; Chagarov, E. A.; Holland, M.; Droopad, R.; Shen, J.; Kummel, A. C., *J. Chem. Phys.* **2010,** *133* (15).

(35) Mack, J. F.; Van Stockum, P. B.; Yemane, Y. T.; Logar, M.; Iwadate, H.; Prinz, F. B., *Chem. Mater.* **2012,** *24* (22), 4357-4362.

(36) Diebold, U., *Surf. Sci. Rep.* **2003,** *48*, 53-229.

(37) Wendt, S.; Schaub, R.; Matthiesen, J.; Vestergaard, E. K.; Wahlstrom, E.; Rasmussen, M. D.; Thostrup, P.; Molina, L. M.; Laegsgaard, E.; Stensgaard, I.; Hammer, B.; Besenbacher, F., *Surf. Sci.* **2005,** *598* (1-3), 226-245.

(38) Park, J. B.; Conner, S. F.; Chen, D. A., *J. Phys. Chem. C* **2008,** *112* (14), 5490-5500.

(39) Wang, H. F.; Ariga, H.; Dowler, R.; Sterrer, M.; Freund, H. J., *J. Catal.* **2012,** *286*, 1-5.

(40) Xu, C.; Lai, X.; Zajac, G. W.; Goodman, D. W., *Phys. Rev. B* **1997,** *56* (20), 13464-13482.

(41) Bredow, T.; Pacchioni, G., *Surf. Sci.* **1999,** *426* (1), 106-122.

(42) Goldstein, D. N.; George, S. M., *Appl. Phys. Lett.* **2009,** *95* (14).

(43) Ahdjoudj, J.; Minot, C., *Catal. Lett.* **1997,** *46* (1-2), 83-91.

(44) Sanz, J. F.; Marquez, A., *J. Phys. Chem. C* **2007,** *111* (10), 3949-3955.

(45) Goldstein, D. N.; George, S. M., *Thin Solid Films* **2011,** *519* (16), 5339-5347.

(46) Kresse, G.; Furthmuller, J., *Comput. Mater. Sci.* **1996,** *6* (1), 15-50.

(47) Kresse, G.; Hafner, J., *Phys. Rev. B* **1993,** *47* (1), 558-561.

(48) Blochl, P. E., *Phys. Rev. B* **1994,** *50* (24), 17953-17979.

(49) Kresse, G.; Joubert, D., *Phys. Rev. B* **1999,** *59* (3), 1758-1775.

(50) Perdew, J. P.; Burke, K.; Ernzerhof, M., *Phys. Rev. Lett.* **1996,** *77* (18), 3865-3868.

(51) Methfessel, M.; Paxton, A. T., *Phys. Rev. B* **1989,** *40* (6), 3616-3621.

(52) Monkhorst, H. J.; Pack, J. D., *Phys. Rev. B* **1976,** *13* (12), 5188-5192.

(53) Morgan, B. J.; Watson, G. W., *J. Phys. Chem. C* **2009,** *113* (17), 7322-7328.